Remarked Suppression of $A\beta_{42}$ Protomer-Protomer Dissociation Reaction via Pentamer Dimerization

Ikuo Kurisaki[*1], Shigenori Tanaka[*1]

[1]Department of Computational Science, Graduate School of System Informatics, Kobe University, 1-1 Rokkodai-cho, Nada-ku, Kobe 657-8501, Japan

[*]Ikuo Kurisaki

E-mail: kurisaki@bear.kobe-u.ac.jp, Tel: +81-78-803-6472

[*]Shigenori Tanaka

E-mail: tanaka2@kobe-u.ac.jp, Tel: +81-78-803-6620

Abstract

Multimeric protein complexes are molecular apparatuses to regulate biological systems and often determine their fate. Among proteins forming such molecular assemblies, amyloid proteins have drawn attention over a half-century since amyloid fibril formation of these proteins is supposed to be a common pathogenic cause for neurodegenerative diseases. This process is triggered by the accumulation of fibril-like aggregates, while the minimum size of such aggregate cores remains elusive. We addressed this problem by employing atomistic molecular dynamics simulations for the paradigmatic amyloid protein, amyloid-β (1-42) ($A\beta_{42}$). Seven different dimeric forms of oligomeric $A\beta_{42}$ fibril-like aggregate in aqueous solution, ranging from tetramer to decamer, were considered. We found effects of the size of these fibril-like aggregates on their thermodynamic stability and have clarified kinetic suppression of protomer-protomer dissociation reactions even at the point of pentamer dimer formation, where the theoretically estimated reaction time exceeds the lifetime of human beings. $A\beta_{42}$ pentamer appears in the size range of experimentally observed $A\beta_{42}$ aggregates. Then, we could suppose that the stable formation of fibril-like $A\beta_{42}$ pentamer species is involved in a turning point where rapid growth of $A\beta_{42}$ amyloid fibrils is triggered. A similar relationship between the oligomer size and the thermodynamic stability may hold to other amyloid fibril formations and

multimeric protein assemblies via nuclei formation, for example, actin and tubulin filament elongation processes.

Introduction

Biological events essential for cell survival are brought about through assembly and disassembly of multiple proteins (1,2). To understand how these multimeric protein complexes function inside the cell, physicochemical characterization of their formation mechanism is indispensable. It is becoming more feasible to directly examine the problems due to technical developments in the last two decades (3,4), whereas the comprehensive knowledge has not yet been obtained satisfactorily.

Amyloid is one of homomeric forms of protein assembly, often referred to as protein aggregates, and has been widely observed in biological systems. Such aggregate products are classified into the two categories, functional amyloid and pathogenic amyloid. (5) In particular, the latter have drawn much attention because they are supposed as causes of several neurodegenerative diseases, such as Alzheimer and Parkinson diseases. (6)

Since suppression of amyloid formation is considered as practical therapeutic strategy for these serious diseases, (7,8) molecular mechanisms for their formation have been extensively studied. (9-11) It is supposed that amyloid fibril formation proceeds via the consecutive three phases. Firstly, monomers assemble to make repertoire of oligomers; a part of oligomers assumes fibril-like, growth-competent aggregates referred to as growth nuclei (lag phase). (12,13) Secondly, growth nuclei species associate with each other to

make larger protofibrils while they convert natively folded monomers into growth-competent monomers to enhance rapid fibril formation (growth phase). Finally, fibril growth processes are balanced with fibril decomposition processes, then reaching thermal equilibrium and completing fibril formation (plateau phase).

In particular, the progress from lag phase to growth phase plays a critical role in an amyloid fibril formation. Sufficient amounts of growth nuclei species are formed in the lag phase (14), then triggering amyloid fibril growth (13). The molecular entity of growth nuclei is regarded as fibril-like aggregates. (13) Thus clarifying the minimum size of thermodynamically stable fibril-like aggregates, which can be involved in amyloid fibril growth, is a landmark to understand molecular mechanisms for the shift from lag phase to growth phase.

In this context, earlier studies on amyloid-β (1-42) ($A\beta_{42}$) have discussed the functional roles of oligomeric aggregates as growth nuclei in amyloid fibril growth, for example. (15-17) Nontheless, the minimum size of growth nuclei species remains to be elucidated so far even for the paradigmatic amyloid protein. Solving the problem appears to be difficult due to molecular diversity of $A\beta_{42}$ aggregates found in lag phase (18-21). It is still challenging for experimental approaches to separately examine physicochemical characters of individual oligomeric aggregate species. Under these circumstances, an

experimental study reported that $A\beta_{42}$ oligomers take fibril forms in the aqueous solution (15), suggesting that such oligomeric $A\beta_{42}$ protomers contribute to the formation of growth nuclei species.

Then, we address to reach the landmark knowledge with employing atomistic molecular dynamics simulations for oligomeric $A\beta_{42}$ protomers. This study starts from confirming the conjecture made in our earlier study (22): $A\beta_{42}$ protomer growth results in suppression of conformational fluctuation such as inter-$A\beta_{42}$ protomer twisting and then thermodynamically stabilizes $A\beta_{42}$ fibril-like aggregates. We made this conjecture from the observation that structural fluctuation destabilizes $A\beta_{42}$ protomer dimer formation.

The seven $A\beta_{42}$ protomer dimers in aqueous solution are considered as models of $A\beta_{42}$ fibril-like aggregates, where the size of $A\beta_{42}$ protomer ranges from tetramer to decamer. We then examine conformational fluctuation and dissociation free energies of these $A\beta_{42}$ protomer dimers, aiming to identify the minimum species of irreversibly formed fibril-like $A\beta_{42}$ aggregate within mean lifetime of human beings.

We then observed kinetic inactivation of protomer-protomer dissociation reactions even for $A\beta_{42}$ pentamer dimer. It is noted that $A\beta_{42}$ pentamer is found in the range of size of experimentally observed soluble $A\beta_{42}$ oligomers (15,23), and such small oligomeric aggregates are supposed to promote amyloid fibril formation by functioning as secondary

nucleation competent aggregates (15). Our observation then suggests that stable formation of this protomer species is involved in a turning point in $A\beta_{42}$ amyloid fibril formation processes, then giving an important clue toward comprehensive understanding of microscopic mechanisms for shift from the lag phase to the growth phase.

Materials and Methods

Setup of amyloid-β (1-42) protomer dimer systems

We used the cryo-electron microscopy (cryo-EM) structure (PDB entry: 5OQV (24)) to construct amyloid-β (1-42), $A\beta_{42}$, protomer dimer systems; a protomer denotes an $A\beta_{42}$ oligomer composed of $A\beta_{42}$ monomers with growth-competent conformation. There is another full-length $A\beta_{42}$ fibril structure (PDB entry: 2NAO (25)), while we selected this structure by considering the relationship with our earlier study (22).

Here we consider dimer of *N*-mer $A\beta_{42}$ protomer as the model of fibril-like aggregate, where the value of *N* ranges 4 to 10 (**Figure 1**). Each of the seven models is annotated by $A\beta_{42}$(N:N) or simply N:N, hereafter. Nε protonation state was employed for each of histidine residues, and all carboxyl groups in aspartate and glutamate residues were set to the deprotonated state. Employing each of the seven $A\beta_{42}$(N:N), we prepared seven $A\beta_{42}$ protomer dimer systems, whose annotations and molecular components are summarized

in **Table 1**. Since we are interested in relationship between size and thermodynamic stability for these $A\beta_{42}$ protomers, no biological co-solutes were added into aqueous solution except for the counter ions to electronically neutralize these molecular systems. The additional detail for system construction is described in Supporting Information (see **SI-1**).

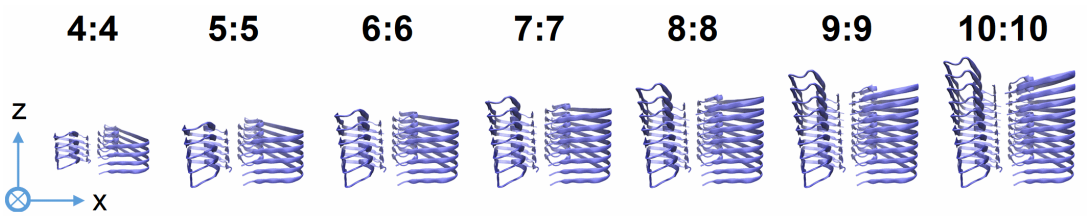

Figure 1. Molecular structures of $A\beta_{42}$ protomer dimers. Each of two integers separated by colon denotes the number of $A\beta_{42}$ monomer in the protomer. The X and Z axes are shown on this plane. The cross in circle denotes Y-axis which directs from this surface to the back.

Table 1. Molecular components of $A\beta_{42}$ protomer dimer systems employed for the molecular dynamics simulations.

size of $A\beta_{42}$ protomer	number of K^+ cations	number of water molecules	box axis length [Å]		
			x	y	z
4	24	33406	138.4	104.2	78.4
5	30	35679	139.1	105.4	83.3
6	36	38153	139.8	106.0	87.7
7	42	41156	140.5	106.9	92.5
8	48	42498	140.6	107.4	96.8
9	54	44855	141.5	108.4	101.7
10	60	46828	141.6	109.2	106.4

To calculate the forces acting among atoms, AMBER force field 14SB (26), TIP3P water model (27,28), and JC ion parameters adjusted for the TIP3P water model (29,30) were used for amino acid residues, water molecules, and ions, respectively. Molecular modeling of each $A\beta_{42}$(N:N) system was performed using the LEaP modules in AmberTools 17 package (31).

Simulation setup

Molecular mechanics (MM) and molecular dynamics (MD) simulations were performed under the periodic boundary condition with GPU-version PMEMD module in

AMBER 17 package (31) based on SPFP algorism (32) with NVIDIA GeForce GTX1080 Ti. Electrostatic interaction was treated by the Particle Mesh Ewald method, where the real space cutoff was set to 9 Å. The vibrational motions associated with hydrogen atoms were frozen by SHAKE algorithm through MD simulations. The translational center-of-mass motion of the whole system was removed by every 500 steps to keep the whole system around the origin, avoiding an overflow of coordinate information from the MD trajectory format. These simulation conditions mentioned above were common in all of the simulations discussed in this manuscript.

Unbiased molecular dynamics simulation

Following temperature relaxation NVT simulations, 30-ns NPT MD simulations (300 K, 1 bar) were performed and used for following analyses. The system temperature and pressure were regulated with Berendsen thermostat (33) with a 5-ps of coupling constant and Monte Carlo barostat with attempt of system volume change by every 100 steps, respectively. A set of initial atomic velocities was randomly assigned from the Maxwellian distribution at 0.001 K at the beginning of the NVT simulations. The time step of integration was set to 2 fs. For each $A\beta_{42}$ fibril system, this simulation procedure was repeated thirty times by assigning different initial atomic velocities. The further

details are shown in Supporting Information (see **SI-2**).

Steered and umbrella sampling molecular dynamics simulations

Dissociation processes of $A\beta_{42}$ monomer or $A\beta_{42}$ protomer were described by combining a steered molecular dynamics (SMD) simulation with umbrella sampling molecular dynamics (USMD) simulations. The definitions for reaction coordinates for both SMD and USMD simulations are given in Results and Discussion section.

SMD was employed to dissociate an $A\beta_{42}$ monomer or protomer from the remaining part of $A\beta_{42}$(N:N). 0.25-ns SMD simulation was carried out under constant NPT condition (300 K, 1 bar), where the system temperature and pressure were regulated by Langevin thermostat with 1-ps^{-1} collision coefficient, and Monte Carlo barostat with attempt of system volume change by every 100 steps, respectively. The value of reaction coordinate was gradually changed through the SMD simulations by imposing the harmonic potential with the force constant of 100 kcal/mol/$Å^2$.

Then, certain numbers of snapshot structures were extracted from the SMD trajectory and employed for USMD windows. Following temperature relaxation simulations, several nanosecond NVT USMD simulations (300 K) were performed for each of the USMD windows (**Table S1** and **Tables S2-3** in Supporting Information for $A\beta_{42}$ protomer

dissociation and $A\beta_{42}$ monomer dissociation, respectively). The system temperature was regulated using Langevin thermostat with 1-ps^{-1} collision coefficient. Each of the last 1-ns USMD trajectories was used to construct a potential of mean force.

This combined SMD-USMD procedures are repeated eight times for each $A\beta_{42}$ protomer dimer system. Sets of initial atomic coordinates for SMD simulations were randomly selected from the thirty set of unbiased 30-ns NPT MD simulations without allowing duplication. The further details are illustrated in Supporting Information (see **SI-3**).

Trajectory analyses

Dihedral angle, hydrogen bond (HB) formation and root mean square deviation (RMSd) were calculated with the cpptraj module in AmberTools 17 package (31). We calculated RMSd to the cryo-EM derived $A\beta_{42}$ protomer dimer structure (24) using the backbone heavy atoms (i.e., C_α, N, C and O). The geometrical criterion of HB formation is as follows: H-X distance was < 3.5 Å and X-H-Y angle was > 120˚, where X, Y and H denote acceptor, donor and hydrogen atoms, respectively.

Each set of USMD trajectories was used to calculate potential of mean force (PMF) with Weighed Histogram Analysis Method (WHAM)(34,35). Statistical errors of PMF

values, $\sigma_{PMF}(\xi)$, were estimated by employing bootstrapped sampling (36):

$$\sigma_{PMF}(\xi) = \left[(N_b - 1)^{-1} \sum_{k=1}^{N_b} \left(W_{b,k}(\xi) - \langle W_b(\xi) \rangle \right)^2 \right]^{\frac{1}{2}} \quad (1)$$

Here, N_b, ξ, and $W_{b,k}(\xi)$ denote the number of bootstrapped sampling, the reaction coordinate and the value of kth bootstrapped potential of mean force at each point of ξ, respectively. $\langle W_b(\xi) \rangle$ is average over all $W_{b,k}(\xi)$, where the value of N_b is set to 200.

Reaction rate, k_{TST}, is estimated by using Eyring's transition state theory:

$$k_{TST} = \frac{k_B T}{h} \exp\left(\frac{-\Delta F^{\dagger}}{k_B T} \right) \quad (2)$$

Here, $\Delta F^{\dagger}$, h, k_B and T denote an activation barrier height, Planck constant, Boltzmann constant and a temperature of system, respectively. Reaction time scale, τ_{TST}, is defined as the inverse of k_{TST}. $\Delta F^{\dagger}$ is defined as $F(\xi_0') - F(\xi_0)$, where PMF has local minimum at ξ_0, and gradient of PMF turns from positive to negative values at ξ_0', which is greater than ξ_0. The estimation with employing Eq. 2 is supposed to be an upper bound of the reaction rate (or a lower bound of the reaction time) (37,38) and we accordingly remarked the influence on each of observations we obtained (see related discussion in Results and Discussion section).

Molecular structures were illustrated using Visual Molecular Dynamics (VMD). (39) Error bars are calculated from standard error and indicate 95% confidence interval if there

is no annotation.

Results and Discussion

Inter-Aβ_{42} protomer twisting is suppressed through fibril growth

We examined conformational fluctuation of Aβ_{42} protomer dimers under thermal noise by employing each thirty sets of 30-ns unbiased NPT MD simulations. **Figure 2** shows time-course change of averaged RMSd values for Aβ_{42} protomer dimers. For each of the seven systems, it can be considered that the values reach convergence after 20 ns so that we suppose that conformation of each Aβ_{42} protomer dimer is relaxed under aqueous condition. Larger protomer dimers have smaller converged RMSd values, suggesting suppression of conformational fluctuation through increasing sizes of protomers. Aβ(4:4) system shows relatively large RMSd fluctuation compared with the other six systems. Nonetheless, the fluctuation is in magnitude of c.a. 0.2 Å within the time domain and seems smaller than atomic scales, then possibly being insignificant. Accordingly, we employed partial MD trajectories in the period after 20 ns for following analyses.

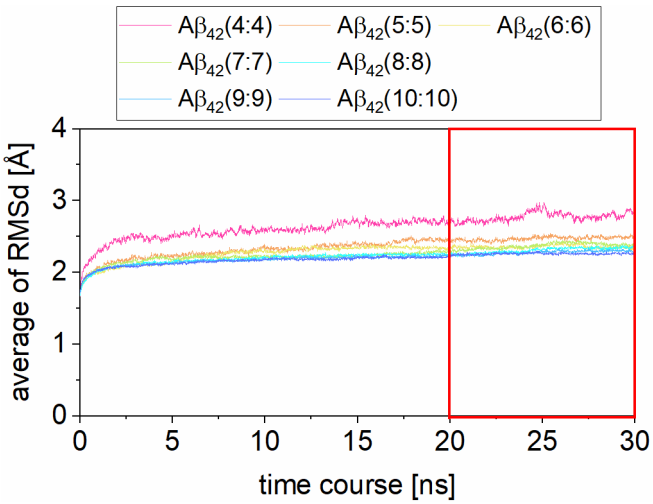

Figure 2. Time-course analyses of root mean square deviation (RMSd). Each result of Aβ$_{42}$ protomer dimer systems is distinguished by color. The time domain supposed as convergence is indicated by the red rectangle.

Recalling the effect of Aβ$_{42}$ protomer size on the conformational fluctuation of Aβ$_{42}$ protomer dimers, we examined inter-Aβ$_{42}$ protomer twisting angle (θ_T) (**Figure 3A**). This θ_T is defined as the dihedral angle in the manner similar to that in our earlier study (22). **Table 2** gives statistical analyses for values of θ_T calculated for each of the seven systems. We could not find significant difference in averaged value of θ_T among the seven systems. Meanwhile, standard deviation (S. D.) reflects the effect of protomer size; Aβ$_{42}$(4:4) shows larger S. D. of θ_T than the other systems.

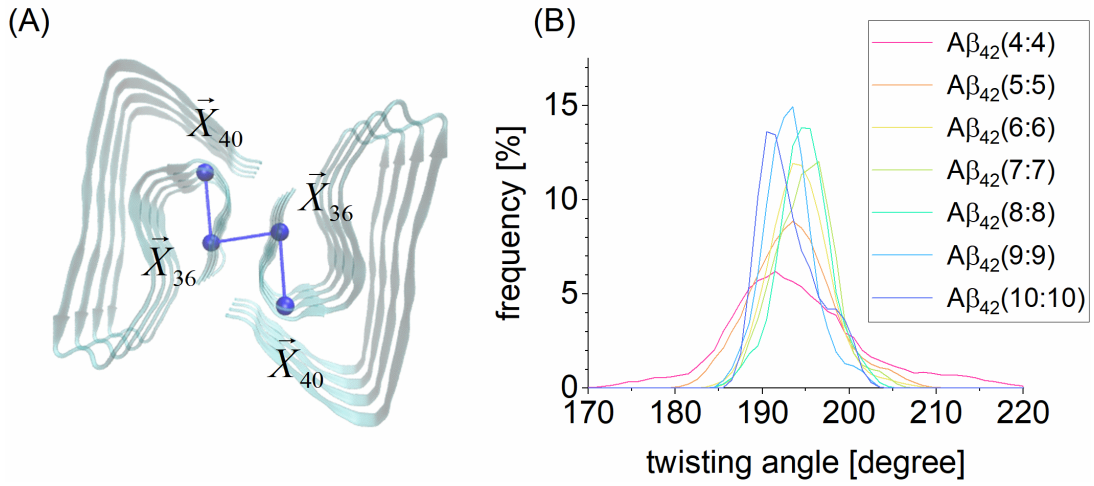

Figure 3. Inter-Aβ$_{42}$ protomer twisting angle. (A) illustration of the twisting angle. (B) twisting angle distributions for each Aβ$_{42}$ protomer dimer system. In panel A, $\vec{X}_m$ denotes the coordinate averaged for the C$_\alpha$ atoms of the mth residues in a Aβ$_{42}$ monomer over the protomer (shown with blue ball); Aβ$_{42}$(4:4) is illustrated here as an example. In panel B, each result of Aβ$_{42}$ protomer dimer systems is distinguished by color, and bin width is set to 1°.

Table 2. Statistical analyses of inter-Aβ_{42} protomer twisting angle.

Aβ_{42} protofibril model system	twisting angle [deg.]	
	average ± 2 × S. E.*	S. D.*
Aβ_{42}(4:4)	193.9 ± 2.6	7.1
Aβ_{42}(5:5)	193.5 ± 1.5	4.0
Aβ_{42}(6:6)	194.3 ± 1.1	2.9
Aβ_{42}(7:7)	194.9 ± 1.1	2.9
Aβ_{42}(8:8)	194.8 ± 1.0	2.7
Aβ_{42}(9:9)	193.1 ± 1.0	2.7
Aβ_{42}(10:10)	193.1 ± 1.2	3.2

*S. E. and S. D. denote standard error and standard deviation, respectively.

Dependence of the S. D. on protomer size can be further clarified by showing the shapes of the distributions of θ_T (**Figure 3B**). That for Aβ_{42}(4:4) shows longer tails (the S.D. value is 7.0 [deg.]) than those for other systems. Comparing Aβ_{42}(5:5) with Aβ_{42}(4:4), the S. D. value shows 1.75-fold decrease, for example. We can find further localization of distributions for larger Aβ_{42} protomer dimers, whose S. D. values are c.a. 3.0 [deg.]. These observations clearly indicate that increasing the size of Aβ_{42} protomer results in suppression of inter-protomer rotation. This result validates the former part of our hypothesis that Aβ_{42} protomer growth results in suppression of conformational fluctuation such as inter-Aβ_{42} protomer twisting.

Increase of hydrogen bond formation between the protomers additively changes the height of free barrier of protomer dissociation reaction

We test the latter part of our hypothesis that suppressing conformational fluctuation of $A\beta_{42}$ protomer dimer actually enhances thermodynamic stability of the protomer dimer. A potential of mean force (PMF) was calculated for each of protomer-protomer dissociation reactions, where the distance between centers of mass for each protomer is employed as the reaction coordinates (see **Figure 4A** for the definition).

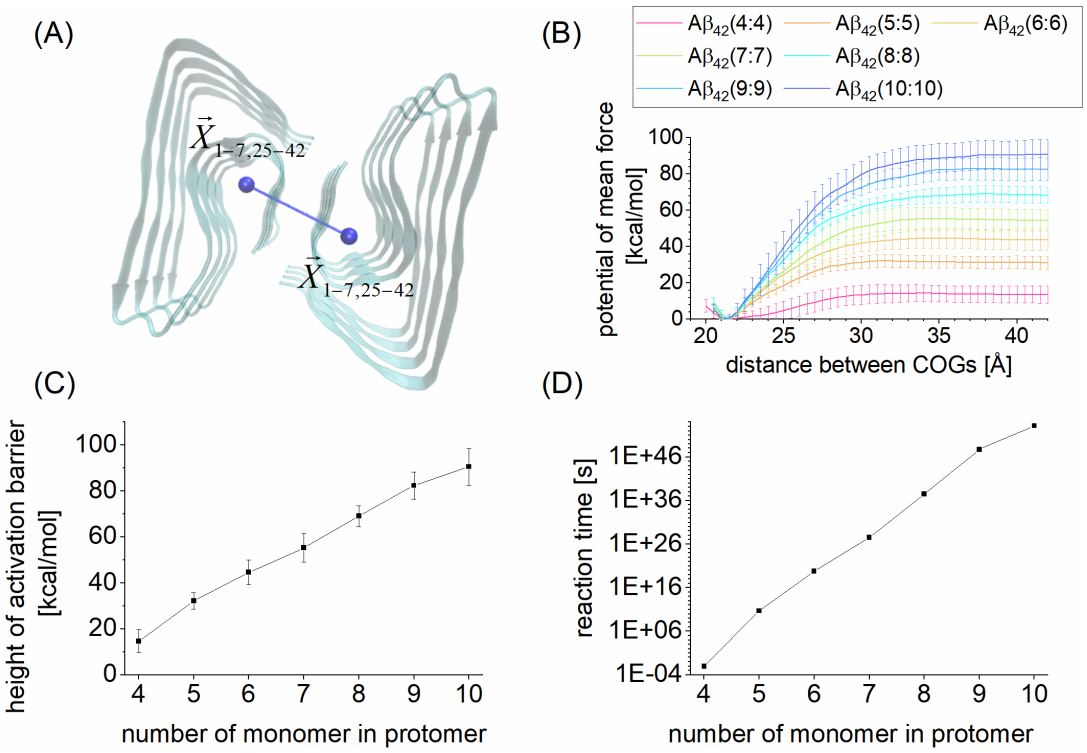

Figure 4. Analyses for Aβ$_{42}$ protomer-protomer dissociation reaction. (A) Illustration of reaction coordinate. (B) Potential of mean forces (PMFs). (C) Height of activation barrier obtained from the PMFs. (D) Reaction time evaluated with Erying's transition state theory. In panel A, $\vec{X}_{m-n,s-t}$ denotes the averaged coordinate (shown with blue ball), which is calculated for the (n−m+1) C$_\alpha$ atoms of the mth, m+1th … nth and sth, s+1th … tth residues in the protomer, and the case of Aβ$_{42}$(4:4) is illustrated here as an example. In panel B, each of Aβ$_{42}$ protomer dimer systems is distinguished by color.

As shown in **Figure 4B**, each of the PMFs has one activation barrier toward the dissociation direction, appearing to be uphill. Furthermore, the height of activation barrier clearly increases with the size of protomer, thus corroborating the latter part of our

hypothesis (**Figure 4C**).

This change can be explained by considering the number of hydrogen bond (HB) formation between the protomers. **Figure 4C** and **Figure 5A** show the height of activation barrier and the number of inter-Aβ_{42} protomer HB, which is calculated by using both backbone and sidechain atoms in Aβ_{42} monomers, respectively. We can find that both of these two quantities additively change according to protomer size and it thus could be said that increase of the protomer size directly contributes to enthalpic stabilization of Aβ_{42} protomer dimers and suppresses inter-protomer rotation. Such an additive change of energetic stability is probably associated with Aβ_{42} aggregation mechanisms via subunit stacking along the fibril axis.

It is worthwhile to note that the number of hydrogen bond formation per Aβ_{42} monomer ($n_{monomer}^{HB}$) seems to converge up to Aβ_{42}(8:8) (**Figure 5B**): $n_{monomer}^{HB}$ shows apparent monomer size-dependence by Aβ_{42}(7:7), while the variable seems to become monomer size-independent from Aβ_{42}(8:8). This observation let us suggest that Aβ_{42}(8:8) is a boundary where a flexible fibril-like aggregate converts into solid Aβ_{42} protofibril structure.

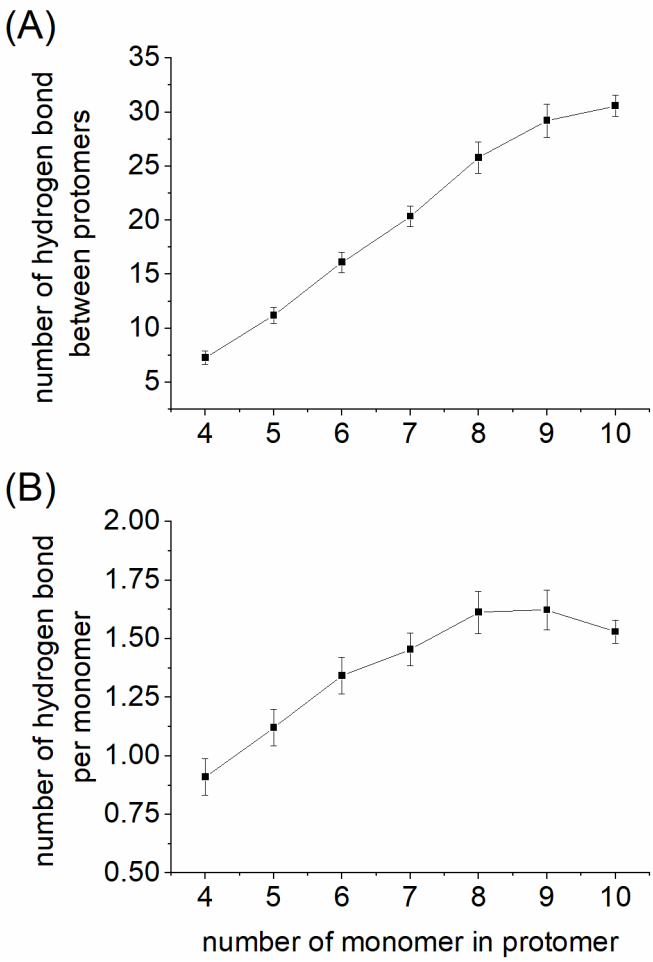

Figure 5. Hydrogen bond (HB) formation between Aβ$_{42}$ protomers. (A) whole number of the HB. (B) the number of HB divided by the number of Aβ$_{42}$ monomer in the Aβ$_{42}$ protomer dimer.

Protomer-protomer dissociation reaction is remarkably suppressed at the point of Aβ$_{42}$ pentamer formation

Using the heights of activation barriers calculated above, we estimated the time scale of protomer dissociation reactions (τ [s]) (**Figure 4D**). From the biological point of view, it is worthwhile discussing the difference between that of Aβ$_{42}$(4:4) and Aβ$_{42}$(5:5), in

particular. According to our estimations with Eyring's transition state theory, the value of τ for $A\beta_{42}$(4:4) is 8.8 ms which falls into timescales of cellular processes, while that for $A\beta_{42}$(5:5) is 1680 year which is much longer than mean lifetime of human being. This critical change of the reaction timescale is due to the exponential dependence on activation barrier height in Eq. 2.

The reaction time estimation denotes that the protomer-protomer dissociation reaction is kinetically suppressed in decomposition processes of $A\beta_{42}$(5:5) and also in those of greater protomer dimers. Since Eyring's transition state theory would often underestimate reaction timescales, (37,38) correction of such underestimation might indicate that oligomeric species smaller than $A\beta_{42}$(5:5), *e.g.*, $A\beta_{42}$(4:4), show suppression of inter-protomer dissociation as well. Nonetheless, the observation results for suppression of inter-$A\beta_{42}$ protomer dissociation within mean lifetime of human being would remain unchanged essentially.

The above insight, which is obtained by considering the seven model systems of $A\beta_{42}$ fibril-like aggregate under the solvated conditions, supports our conjecture that increasing size of protomer contributes to thermodynamic stability of fibril-like aggregates. Furthermore, suppression of protomer-protomer dissociation route is found for the relatively small protomer dimer, $A\beta_{42}$(5:5).

The recent experimental studies reported that the number of subunits in soluble $A\beta_{42}$ aggregates ranges from 4 to 8 (15,23). Besides, such smaller oligomer species are supposed to be secondary nucleation competent fibril-like aggregates which can convert natively folded monomers into growth-competent monomers. (15) Recalling these two experimental evidences, we could suppose that stable formation of fibril-like $A\beta_{42}$ pentamer species activates secondary nucleation processes, generates additional fibril-like oligomers and accumulate growth nuclei species via dimeric association of this protomer species. This step seems to be involved in an important turning point where the growth phase proceeds from the lag phase.

$A\beta_{42}$ pentamer and its dimeric form may appear without regard to monomer dissociation from the edge of a protomer dimer

It can be assumed that increase of protomer size similarly suppresses an alternative route of $A\beta_{42}$ aggregate decomposition, that is, $A\beta_{42}$ monomer dissociation from the edges of protomers. To examine effects of protomer size on the alternative dissociation route, we analyzed thermodynamic stability of $A\beta_{42}$ monomer on the protomer edge. We calculated potential of mean forces for monomer dissociations from $A\beta_{42}$(4:4) and $A\beta_{42}$(10:10) (**Figure 6A** and **6B**), the smallest and largest protomer dimers examined in

this study, respectively. Besides, recalling that the smallest Aβ$_{42}$ fibril species is composed of 8 monomers or fewer (15), we suppose that Aβ$_{42}$(10:10) is sufficient in size as a model of Aβ$_{42}$ fibril species

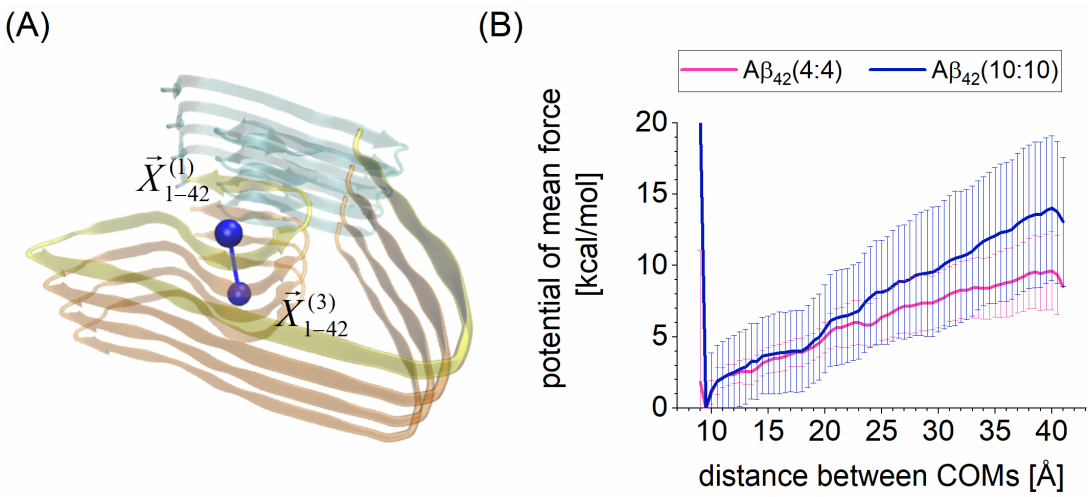

Figure 6. Analyses for Aβ$_{42}$ monomer dissociation reaction. (A) Illustration of reaction coordinate. (B) Potential of mean forces (PMFs). In panel A, $\vec{X}^{(l)}_{m-n}$ denotes the averaged coordinate (shown with blue ball), which is calculated for the (n−m+1) C$_\alpha$ atoms of the mth, m+1th … n^{th} residues for l monomers in the protomer, and the case of Aβ$_{42}$(4:4) is illustrated here as an example. The dissociated monomer and the neighboring trimer is colored by transparent yellow and blue, respectively. In panel B, each of Aβ$_{42}$ fibril-like aggregate systems is distinguished by color.

Each of the PMFs has one activation barrier toward the dissociation direction and the height of activation barrier appears to increase with the size of protomer. However, the

effects of size are not substantial compared with the case of protomer-protomer dissociation (see **Figure 4**). The estimated reaction times are 1.6 μs and 5.9 ms for $A\beta_{42}$(4:4) and $A\beta_{42}$(10:10), respectively.

As discussed above, Eyring's transition state theory would often underestimate the reaction time scales (37,38). Then we here expect how much the values of timescale increase with underestimation correction by referring to earlier kinetic studies on other biomacromolecular processes(40-42). Their underestimation corrections range from 10^1- to 10^6-fold. If we consider the correction for $A\beta_{42}$(10:10) at maximum, the timescale becomes 590 seconds. Meanwhile, the value is still within cellular timescales even for the model of $A\beta_{42}$ fibril species, $A\beta_{42}$(10:10). It thus remains unclear so far whether $A\beta_{42}$ monomer dissociation reactions prevents stable formation of $A\beta_{42}$ amyloid fibril species.

Under this circumstance, it is worthwhile noting the kinetic reaction study by Cohen and co-workers. (10) They reported that $A\beta_{42}$ amyloid fibril formation proceed even if $A\beta_{42}$ monomers can be dissociated from $A\beta_{42}$ fibril species in their kinetic reaction scheme. They gave the reaction timescale of 100 seconds, which is still fallen within cellular timescales and similar in the magnitude to our estimation with the maximum correction. These dissociation reactions may not critically prevent stable formation of $A\beta_{42}$ fibril species.

Additionally, the other experimental study reported presence of oligomeric $A\beta_{42}$ fibril aggregate, where the smallest species is composed of 8 $A\beta_{42}$ monomers or fewer (15). The above PMF analyses indicate that $A\beta_{42}$ protomer size has lesser influence on monomer dissociation from the edge of a protomer dimer; the reaction time scales are still fallen within cellular timescales. Nonetheless, according to the two earlier experimental studies, we can still assume that $A\beta_{42}$ pentamer and the dimeric form, $A\beta_{42}$(5:5), emerge in the process of $A\beta_{42}$ amyloid fibril formation and function as a growth nuclei species.

The above discussion raises a new question which brings us further insights into molecular mechanisms for $A\beta_{42}$ growth nuclei formation. It is noted that the values calculated from our simulations for $A\beta_{42}$(10:10) is smaller by c.a. 10^5 fold than Cohen's estimation (10). We can suppose the two factors to explain this underestimation for the reaction timescale. One is the usage of Eyring's transition state theory, as expected. (37,38) As referred to above, the maximally corrected value is similar to Cohen's estimation. On the other hand, magnitude of correction appears to strongly depend on molecular processes (40-42) and then there is room to discuss whether the underestimation is simply due to the usage of Eyring's transition state theory.

The other possible factor is atomistic interaction of $A\beta_{42}$ fibril-like aggregates with molecular environments. The present study was designed to confirm our conjecture about

the significant effect of sizes of $A\beta_{42}$ protomer on thermodynamic stability of $A\beta_{42}$ fibril-like aggregates, where isolated $A\beta_{42}$ protomer dimers was placed in aqueous solution. Meanwhile, the earlier studies reported fibril-like aggregate formation accompanied by the molecular crowding of $A\beta_{42}$ molecules. (16,17,43) $A\beta_{42}$ crowding may surround an $A\beta_{42}$ monomer on the edge of the $A\beta_{42}$ protomer dimer and configurationally restrict the dissociation pathway, then increasing free energy barrier of the dissociation reaction and supporting the stable formation of minimum $A\beta_{42}$ growth nuclei species.

The later possibility is in particular worth considering preferentially due to the evidence from the experimental observations about $A\beta_{42}$ fibril-like aggregate formation. However, further investigation for this problem is beyond the scope of this study, thus being left for future study.

Concluding Remarks

Clarifying minimum size of growth-competent aggregates is a landmark knowledge to understand molecular mechanisms for amyloid fibril formation. In this context, we considered a paradigmatic amyloid protein, $A\beta_{42}$, and examined effects of the protomer size on thermodynamic stability of the protomer dimers. We elucidated that even dimer formation of $A\beta_{42}$ pentamer kinetically suppresses this protomer-protomer dissociation

within mean lifetime of human being.

This achievement suggests that, upon directional elongation of protein multimer via nucleation process, a kinetic rate constant can remarkably change by the size of protein assembly to restrict feasible reaction processes. Size dependence of kinetic rate constant has been gradually employed in the recent theoretical studies on kinetics of protein filament formation(44), while the processes in which such dependence is considered are still limited to monomer association and dissociation reactions so far. Our novel achievement may indicate importance of additional description of size dependence to more realistically illustrate filamentous assembly processes in the context of reaction kinetic models.

Our observation about $A\beta_{42}$ pentamer dimer appears to be worth noting when we examine how the growth phase proceeds from the lag phase. $A\beta_{42}$ pentamer is found in the range of size of experimentally-observed soluble $A\beta_{42}$ oligomers (15,23), which are supposed to be secondary nucleation competent aggregates (15). Recalling these experimental evidences, we could suppose that stable formation of $A\beta_{42}$ pentamer is involved in an important turning point where the growth phase proceeds from the lag phase, that is, the important reaction step in progress of $A\beta_{42}$ amyloid fibril growth.

We have here discussed $A\beta_{42}$ protomer systems and provided new insights into

physicochemical mechanism for the $A\beta_{42}$ multimerization process. Meanwhile our theoretical approach can be applicable to studies on polymorphism of Aβ species (21) and other pathogenic amyloid proteins such as prion (45), α-synuclein (46) and fused in sarcoma (FUS) (47). Free energy analyses for these proteins could give a similar observation that dimeric association of oligomeric protomer species is sufficient to inactivate protomer-protomer dissociation route in the decomposition process. Meanwhile it can be assumed that each amyloid protein shows its characteristic protomer size due to the own atomic structure of amyloid fibril-like aggregate.

Our study has started to clarify a significant effect of sizes of $A\beta_{42}$ protomer on thermodynamic stability of $A\beta_{42}$ fibril-like aggregates and then gave a suggestion for an additional key factor for stable formation of minimum $A\beta_{42}$ growth nuclei species. The role of this factor will be examined in future study by considering the effects of molecular crowding milieu on formation of relatively small protomer dimer such as $A\beta_{42}$(5:5) as a model of growth nuclei species.

Supporting Information

The Supporting Information is available. Detailed procedures for unbiased MD, SMD and USMD simulations, Figures and Tables for analyses of these simulations.

Acknowledgements

This work was supported by a Grant-Aid for Scientific Research on Innovative Areas "Chemistry for Multimolecular Crowding Biosystems" (JSPS KAKENHI Grand No. JP17H06353).

Author Information

Corresponding Authors

Ikuo Kurisaki - Graduate School of System Informatics, Kobe University, 1-1 Rokkodai, Nada-ku, Kobe 657-8501, Japan; ORCID: 0000-0003-4519-1093; Email: kurisaki@bear.kobe-u.ac.jp

Shigenori Tanaka - Graduate School of System Informatics, Kobe University, 1-1 Rokkodai, Nada-ku, Kobe 657-8501, Japan; ORCID: 0000-0002-6659-2788; Email: tanaka2@kobe-u.ac.jp

Notes

The authors declare no competing financial interest.

References

1. Bolanos-Garcia, V. M., Q. Wu, T. Ochi, D. Y. Chirgadze, B. L. Sibanda, and T. L. Blundell. 2012. Spatial and temporal organization of multi-protein assemblies: achieving sensitive control in information-rich cell-regulatory systems. *Philos. T. R. Soc. A*. 370:3023-3039, doi: 10.1098/rsta.2011.0268.

2. Marsh, J. A., and S. A. Teichmann. 2015. Structure, dynamics, assembly, and evolution of protein complexes. *Annu. Rev. Biochemistry,* 84:551-575, doi: 10.1146/annurev-biochem-060614-034142.

3. Erba, E. B., L. Signor, and C. Petosa. 2020. Exploring the structure and dynamics of macromolecular complexes by native mass spectrometry. *J. Proteomics*. 222, doi: ARTN 103799 10.1016/j.jprot.2020.103799.

4. Uchihashi, T., and C. Ganser. 2020. Recent advances in bioimaging with high-speed atomic force microscopy. *Biophys. Rev*. 12:363-369, doi: 10.1007/s12551-020-00670-z.

5. Chiti, F., and C. M. Dobson. 2017. Protein misfolding, amyloid formation, and human disease: a summary of progress over the last decade. *Annu. Rev. Biochem*. 86:27-68, doi: 10.1146/annurev-biochem-061516-045115.

6. Chiti, F., and C. M. Dobson. 2006. Protein misfolding, functional amyloid, and

human disease. *Annu. Rev. Biochemistry*. 75:333-366, doi: 10.1146/annurev.biochem.75.101304.123901.

7. Tolar, M., S. Abushakra, and M. Sabbagh. 2020. The path forward in Alzheimer's disease therapeutics: Reevaluating the amyloid cascade hypothesis. *Alzheimers Dement*. 16:1553-1560, doi: 10.1016/j.jalz.2019.09.075.

8. Selkoe, D. J., and J. Hardy. 2016. The amyloid hypothesis of Alzheimer's disease at 25years. *Embo Mol. Med*. 8:595-608, doi: DOI 10.15252/emmm.201606210.

9. Knowles, T. P. J., C. A. Waudby, G. L. Devlin, S. I. A. Cohen, A. Aguzzi, M. Vendruscolo, E. M. Terentjev, M. E. Welland, and C. M. Dobson. 2009. An analytical solution to the kinetics of breakable filament assembly. *Science*. 326:1533-1537, doi: 10.1126/science.1178250.

10. Cohen, S. I. A., S. Linse, L. M. Luheshi, E. Hellstrand, D. A. White, L. Rajah, D. E. Otzen, M. Vendruscolo, C. M. Dobson, and T. P. J. Knowles. 2013. Proliferation of amyloid-β42 aggregates occurs through a secondary nucleation mechanism. *P. Natl. Acad. Sci. USA*. 110:9758-9763

11. Owen, M. C., D. Gnutt, M. M. Gao, S. K. T. S. Warmlander, J. Jarvet, A. Graslund, R. Winter, S. Ebbinghaus, and B. Strodel. 2019. Effects of in vivo conditions on amyloid aggregation. *Chem. Soc. Rev*. 48:3946-3996, doi: 10.1039/c8cs00034d.

12. Harper, J. D., and P. T. Lansbury. 1997. Models of amyloid seeding in Alzheimier's disease and scrapie: Mechanistic truths and physiological consequences of the time-dependent solubility of amyloid proteins. *Annu. Rev. Biochemistry*. 66:385-407, doi: DOI 10.1146/annurev.biochem.66.1.385.

13. Ruggeri, F. S., T. Sneideris, M. Vendruscolo, and T. P. J. Knowles. 2019. Atomic force microscopy for single molecule characterisation of protein aggregation. *Arch. Biochem. Biophys*. 664:134-148, doi: 10.1016/j.abb.2019.02.001.

14. Cohen, S. I. A., M. Vendruscolo, C. M. Dobson, and T. P. J. Knowles. 2012. From macroscopic measurements to microscopic mechanisms of protein aggregation. *J. Mol. Biol*. 421:160-171, doi: 10.1016/j.jmb.2012.02.031.

15. Leppert, A., A. Tiiman, N. Kronqvist, M. Landreh, A. Abelein, V. Vukojević, and J. Johansson. 2021. Smallest secondary nucleation competent Aβ aggregates probed by an ATP-independent molecular chaperone domain. *Biochemistry*. doi: 10.1021/acs.biochem.1c00003.

16. Novo, M., S. Freire, and W. Al-Soufi. 2018. Critical aggregation concentration for the formation of early Amyloid-β (1-42) oligomers. *Sci. Rep-Uk*. 8, doi: ARTN 1783 10.1038/s41598-018-19961-3.

17. Sabate, R., and J. Estelrich. 2005. Evidence of the existence of micelles in the

fibrillogenesis of beta-amyloid peptide. *J. Phys. Chem. B*. 109:11027-11032, doi: 10.1021/jp050716m.

18. Colletier, J. P., A. Laganowsky, M. Landau, M. Zhao, A. B. Soriaga, L. Goldschmidt, D. Flot, D. Cascio, M. R. Sawaya, and D. Eisenberg. 2011. Molecular basis for amyloid-β polymorphism. *Proc. Natl. Acad. Sci U S A*. 108:16938-16943, doi: 10.1073/pnas.1112600108.

19. Hard, T. 2011. Protein engineering to stabilize soluble amyloid β-protein aggregates for structural and functional studies. *Febs J*. 278:3884-3892, doi: 10.1111/j.1742-4658.2011.08295.x.

20. De, S., D. C. Wirthensohn, P. Flagmeier, C. Hughes, F. A. Aprile, F. S. Ruggeri, D. R. Whiten, D. Emin, Z. J. Xia, J. A. Varela, P. Sormanni, F. Kundel, T. P. J. Knowles, C. M. Dobson, C. Bryant, M. Vendruscolo, and D. Klenerman. 2019. Different soluble aggregates of Aβ42 can give rise to cellular toxicity through different mechanisms. *Nat. Commun*. 10, doi: ARTN 1541 10.1038/s41467-019-09477-3.

21. Kollmer, M., W. Close, L. Funk, J. Rasmussen, A. Bsoul, A. Schierhorn, M. Schmidt, C. J. Sigurdson, M. Jucker, and M. Fandrich. 2019. Cryo-EM structure and polymorphism of Aβ amyloid fibrils purified from Alzheimer's brain tissue.

Nat. Commun. 10, doi: ARTN 4760 10.1038/s41467-019-12683-8.

22. Kurisaki, I., and S. Tanaka. 2019. ATP converts Aβ42 oligomer into off-pathway species by making contact with its backbone atoms using hydrophobic adenosine. *J. Phys. Chem. B*. 123:9922-9933, doi: 10.1021/acs.jpcb.9b07984.

23. Wolff, M., B. Zhang-Haagen, C. Decker, B. Barz, M. Schneider, R. Biehl, A. Radulescu, B. Strodel, D. Willbold, and L. Nagel-Steger. 2017. Aβ42 pentamers/hexamers are the smallest detectable oligomers in solution. *Sci. Rep-Uk*. 7, 2493, doi: https://doi.org/10.1038/s41598-017-02370-3

24. Gremer, L., D. Scholzel, C. Schenk, E. Reinartz, J. Labahn, R. B. G. Ravelli, M. Tusche, C. Lopez-Iglesias, W. Hoyer, H. Heise, D. Willbold, and G. F. Schroder. 2017. Fibril structure of amyloid-β(1-42) by cryo-electron microscopy. *Science*. 358:116-119, doi: 10.1126/science.aao2825.

25. Walti, M. A., Ravotti, F., Arai, H., Glabe, C. G., Wall, J. S., Bockmann, A., Guntert, P., Meier, B. H., Riek, R. 2016. Atomic-resolution structure of a disease-relevant Aβ(1-42) amyloid fibril. *P. Natl. Acad. Sci. USA*, 113: E4976-E4984, doi: 10.1073/pnas.1600749113.

26. Maier, J. A., C. Martinez, K. Kasavajhala, L. Wickstrom, K. E. Hauser, and C. Simmerling. 2015. ff14SB: Improving the accuracy of protein side chain and

backbone parameters from ff99SB. *J. Chem. Theory Comput*. 11:3696-3713, doi: 10.1021/acs.jctc.5b00255.

27. Jorgensen, W. L., J. Chandrasekhar, J. D. Madura, R. W. Impey, and M. L. Klein. 1983. Comparison of simple potential functions for simulating liquid water. *J. Chem. Phys*. 79:926-935, doi: 10.1063/1.445869.

28. Kusalik, P. G., and I. M. Svishchev. 1994. The spatial structure in liquid water. *Science*. 265:1219-1221, doi: DOI 10.1126/science.265.5176.1219.

29. Joung, I. S., and T. E. Cheatham. 2008. Determination of alkali and halide monovalent ion parameters for use in explicitly solvated biomolecular simulations. *J. Phys. Chem. B*. 112:9020-9041, doi: 10.1021/jp8001614.

30. Joung, I. S., and T. E. Cheatham, III. 2009. Molecular dynamics simulations of the dynamic and energetic properties of alkali and halide ions using water-dodel-specific ion parameters. *J. Phys. Chem. B*. 113:13279-13290, doi: 10.1021/jp902584c.

31. Amber 17 (University of California, San Francisco, CA).

32. Le Grand, S., A. W. Gotz, and R. C. Walker. 2013. SPFP: Speed without compromise-A mixed precision model for GPU accelerated molecular dynamics simulations. *Comput. Phys. Commun*. 184:374-380, doi: DOI

10.1016/j.cpc.2012.09.022.

33. Berendsen, H. J. C., J. P. M. Postma, W. F. Vangunsteren, A. Dinola, and J. R. Haak. 1984. Molecular-dynamics with couping to an external bath. *J. Chem. Phys*. 81:3684-3690, doi: 10.1063/1.448118.

34. WHAM: the weighted histogram analysis method (University of Rochester Medical Center: Rochester, NY).

35. Kumar, S., D. Bouzida, R. H. Swendsen, P. A. Kollman, and J. M. Rosenberg. 1992. The Weighted histogram analysis method for free-energy calculations on biomolecules. 1. the method. *J. Comput. Chem*. 13:1011-1021, doi: DOI 10.1002/jcc.540130812.

36. Hub, J. S., B. L. de Groot, and D. van der Spoel. 2010. g_wham-f free weighted histogram analysis implementation including robust error and autocorrelation estimates. *J. Chem. Theory Comput*. 6:3713-3720, doi: 10.1021/ct100494z.

37. Case, D. A. 1988. Dynamical simulation of rate constants in protein-ligand interactions. *Prog. Biophys. Mol. Bio*. 52:39-70, doi: Doi 10.1016/0079-6107(88)90007-7.

38. Zhou, H. X. 2010. Rate theories for biologists. *Q. Rev. Biophys*. 43:219-293, doi: 10.1017/S0033583510000120.

39. Humphrey, W., A. Dalke, and K. Schulten. 1996. VMD: Visual molecular dynamics. *J. Mol. Graphics Modell*. 14:33-38, doi: 10.1016/0263-7855(96)00018-5.

40. Roux, B., and M. Karplus. 1991. Ion-transport in a gramicidin-like channel - dynamics and mobility. *J. Phys. Chem*. 95:4856-4868, doi: DOI 10.1021/j100165a049.

41. Dutzler, R., T. Schirmer, M. Karplus, and S. Fischer. 2002. Translocation mechanism of long sugar chains across the maltoporin membrane channel. *Structure*. 10:1273-1284, doi: Pii S0969-2126(02)00811-0

42. Hridya, V. M., J. T. Hynes, and A. Mukherjee. 2019. Dynamical recrossing in the intercalation process of the anticancer agent proflavine into DNA. *J. Phys. Chem. B*. 123:10904-10914, doi: 10.1021/acs.jpcb.9b08470.

43. Lomakin, A., D. S. Chung, G. B. Benedek, D. A. Kirschner, and D. B. Teplow. 1996. On the nucleation and growth of amyloid β-protein fibrils: detection of nuclei and quantitation of rate constants. *P. Natl. Acad. Sci. USA*. 93:1125-1129, doi: DOI 10.1073/pnas.93.3.1125.

44. Šarić, A., Michael, TCT., Zaccone, A., Knowles, TPJ. Frenkel, D. 2016. Kinetics of spontaneous filament nucleation via oligomers: Insights from theory and

simulation. *J. Chem. Phys*. 145, doi: 10.1063/1.4965040.

45. Glynn, C., M. R. Sawaya, P. Ge, M. Gallagher-Jones, C. W. Short, R. Bowman, M. Apostol, Z. H. Zhou, D. S. Eisenberg, and J. A. Rodriguez. 2020. Cryo-EM structure of a human prion fibril with a hydrophobic, protease-resistant core. *Nat. Struct. Mol. Biol*. 27: 417-423, doi: 10.1038/s41594-020-0403-y.

46. Tuttle, M. D., G. Comellas, A. J. Nieuwkoop, D. J. Covell, D. A. Berthold, K. D. Kloepper, J. M. Courtney, J. K. Kim, A. M. Barclay, A. Kendall, W. Wan, G. Stubbs, C. D. Schwieters, V. M. Y. Lee, J. M. George, and C. M. Rienstra. 2016. Solid-state NMR structure of a pathogenic fibril of full-length human alpha-synuclein. *Nat. Struct. Mol. Biol*. 23:409-415, doi: 10.1038/nsmb.3194.

47. Murray, D. T., M. Kato, Y. Lin, K. R. Thurber, I. Hung, S. L. McKnight, and R. Tycko. 2017. Structure of FUS protein fibrils and its relevance to self-assembly and phase separation of low-complexity domains. *Cell*. 171:615-627, doi: 10.1016/j.cell.2017.08.048.
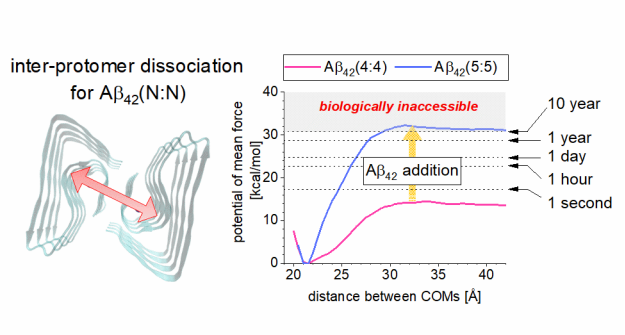
For TOC graphics only